Research Article Vol. 30, No. 13 / 20 Jun 2022 / *Optics Express* 22986

Optics EXPRESS

Cyclic silicon waveguide four-mode converter for mode division multiplexing transmission

Zhe Yuan, Yongchen Wang, Hangming Fan, Ziheng Zhang, Mengfan Cheng, Qi Yang, Ming Tang, Deming Liu, and Lei Deng*

Wuhan National Laboratory for Optoelectronics and School of Optical and Electronic Information, Huazhong University of Science and Technology, Wuhan 430074, China
denglei_hust@mail.hust.edu.cn

Abstract: In this paper, a novel cyclic mode converter (CMC) is proposed and fabricated to implement cyclic mode permutation (CMP) on-chip for differential mode delay and mode-dependent loss elimination in the mode division multiplexing (MDM) transmission system. Cascaded by three optimally designed mode converters that do not affect the non-target modes, the proposed CMC can realize the conversion of any input mode among the $TE_0/TE_1/TM_0/TM_1$ modes. The three-dimensional finite-difference time-domain (3D-FDTD) simulation results show that the insertion loss of our device is less than 0.59 dB, and the crosstalk of each mode is lower than −15 dB under the range of 1500–1600 nm. The flat spectral response of this CMC is maintained even in the presence of fabrication errors up to±10 nm, showing great robustness. The experimental results also prove that at the center wavelength of 1550 nm the measured insertion loss of each mode is below 2.22 dB, and the crosstalk of each mode is lower than −15 dB. The proposed CMC provides a new idea for effectively reducing link damage in the MDM transmission system.

1. Introduction

The increasing demand for communication capacity has made research efforts in space division multiplexing (SDM) transmission become one of the attractive technologies in the future optical fiber communication system [1]. As a kind of SDM technique, the mode division multiplexing (MDM) technology that simultaneously transmits multiple data streams over multi-mode fibers or few-mode fibers (FMFs) is widely concerned. The first long-distance MDM transmission using 3 spatial modes to transmit over 1000 km is reported in [2]. The dominant performance limiting factors in long-distance MDM transmission is the accumulation of differential mode delay (DMD) and the equalization of mode-dependent loss (MDL). In weakly coupled long-distance FMF transmission, DMD and MDL grow almost linearly with fiber length [3,4], which limits the achievable information capacity. Therefore, when the widely-used conventional linear multiple-input multiple-output digital signal processing (MIMO-DSP) algorithm is used at the receiver, the required number of equalizer taps increases sharply [5,6]. Alternatively, the use of special core structures, such as ring core [7,8] and nanopore-assisted core [9], can effectively reduce the impact of DMD and MDL. Nevertheless, high doping difficulty limits the production process, and fabrication tolerance also has a great impact on fiber performance.

A novel cyclic mode permutation (CMP) technique [10] has been proposed recently for 3500 km DMD-unmanaged 6-mode-multiplexed transmission. A threefold recirculating loop system is constructed to transmit signals carried by spatial mode. In this CMP transmission strategy, spatial channels are cyclically interchanged in each span via a pair of mode multiplexers (MUX) and demultiplexers (DEMUX). It seems to provide a new path to decrease the impact of DMD and MDL. Nevertheless, when it comes to the actual transmission link, a large number of MUX need to be deployed in the link at the same distance, which means that the performance of

#463024
Journal © 2022

https://doi.org/10.1364/OE.463024
Received 3 May 2022; revised 1 Jun 2022; accepted 1 Jun 2022; published 8 Jun 2022

mode-(DE)MUX will directly affect the performance of the MDM transmission system. On the other hand, the use of mode-(DE)MUX will increase the cost and occupy a larger space. Lots of mode-(DE)MUX have been reported to realize an MDM system now, such as the free-space optical devices [11], the photon lantern [12], and the multi-plane light conversion (MPLC) [13]. However, they cannot balance performance, cost, and size at the same time. For example, the free-space optical devices, which are easy to design, usually use multiple beam splitters to multiplex spatial modes, thus introducing excess loss. Besides, different modal sets require specific beam structures and transmitter/receiver equipment, which makes the system complex and less compatible. The photon lantern can be well compatible with the optical fiber with low insertion loss, but the crosstalk performance of the current commercial photon lantern devices is generally poor. As an emerging technology, the MPLC can achieve accurate light wave field operations and has the potential to expand the number of mode channels. However, its insertion loss performance needs to be improved at present. At the same time, it puts high demands on optimization algorithms and computational costs. Therefore, suitable methods are highly desired to apply CMP technology to the actual deployment of future MDM transmission systems. Coincidentally, when we focus on one of the threefold recirculating loops in the CMP scheme, the spatial mode carrying MDM signals seems to be converted into another mode every circulation of the loop. It represents that using mode converters to realize CMP operation is a method worthy of consideration.

Driven by the urgent demand for applications in low cost, low loss, high level of integration, high-bandwidth interconnects, and the compatibility with complementary metal-oxide-semiconductor (CMOS) processes, multimode manipulation in silicon photonics is one of the most promising technologies to accommodate the demand for MDM system. Lots of functional devices have been reported to use in MDM systems, such as mode-(DE)MUX [14], multimode waveguide crossings [15], multimode Bragg gratings [16], multimode switching [17], multimode filtering [18], multimode grating coupler [19] and reconfigurable multimode devices [20]. As a key component of MDM operation, mode converters have been extensively researched recently. Different structures for mode converters have been reported, and three methods are mainly used to achieve mode conversions: phase matching [14,21], coherent scattering [22], and beam shaping [20,23]. Based on the powerful mode manipulation capabilities and potentiality for integration with other devices of the mode converter, we think it is a good idea to use cyclic mode converters (CMC) to implement CMP technology on-chip.

In this work, we have developed a novel scheme to implement CMP operation on-chip with a cyclic silicon waveguide mode converter for the first time. Through the theoretical analysis and simulation, the optimally designed cascaded mode converter can realize the conversion of any input mode among the TE_0/TE_1/TM_0/TM_1 modes. The simulation results show that the insertion loss of each mode of our device is less than 0.59 dB and the crosstalk is lower than −15 dB under the range of 1500–1600 nm. In our experiment, a four-mode CMC is successfully fabricated, and its effective length is less than 200 µm. At the center wavelength of 1550 nm, the insertion loss of each mode is below 2.22 dB, and the crosstalk of each mode is less than −15 dB. Besides, when the crosstalk is less than −10 dB, all of the mode bandwidth range is larger than 20 nm. This work expands the design ideas for reducing DMD and MDL in MDM systems, paving the way toward the practical application of silicon-based devices to MDM transmission systems.

2. Principle

Figure 1(a) displays the situation in that four-mode signals transmit over FMF without CMCs deployed in the link. Under the influence of DMD, the pulse broadening for MDM signals causes the mode transmitted in the channel to reach the receiver at different times, which enhances the computational complexity of the MIMO algorithm at the receiver. The CMP scheme in the FMF link can alleviate the damage of DMD and MDL, but the transmission performance will be affected by the excess insertion loss and crosstalk introduced by mode-(DE)MUX, as shown in Fig. 1(b). Figure 1(c) shows the schematic diagram of the proposed long-distance FMF transmission using CMCs. After the four-mode signals transmitting through each CMC, each mode will be converted to a unique corresponding mode. In this transmission strategy, the information symbols delivered on each spatial channel will periodically traverse all optical paths characterized by each spatial mode after four CMCs. Therefore, DMD and MDL caused by different spatial modes will be equated in each channel. Compared with the CMP scheme, our scheme using CMC avoids placing multiple pairs of mode-(DE)MUX in the optical fiber link, which greatly reduces the device cost and link complexity and improves transmission quality at the same time. Meanwhile, most reported mode converters focus on the conversion process between two specified modes. Other mode-conversion processes require changes in the structure and parameters of the converter, which limits the spatial channel expansion in MDM systems. This CMC expands the number of modes up to four and has the potential to extend to more modes with further improvement. Figure 1(d) shows a schematic diagram of the proposed CMC, which is based on the 340 nm thick silicon platform surrounded by a silicon dioxide (SiO_2) upper cladding and buried oxide (BOX) layer. Si and SiO_2 refractive indexes are $n_{Si}(\lambda_0)$ 3.476 and $n_{SiO2}(\lambda_0)$ 1.444 at the central wavelength of $\lambda_0 = 1550$ nm. This CMC is composed of three cascaded mode converters, which are the TE mode-order converter, TE_1-TM_0 polarization rotator (PR), and TM mode-order converter. Compared with many mode converters [24,25] reported previously that may have unexpected effects on the mode of another polarization, these converters only convert the specific modes but do not affect other modes.

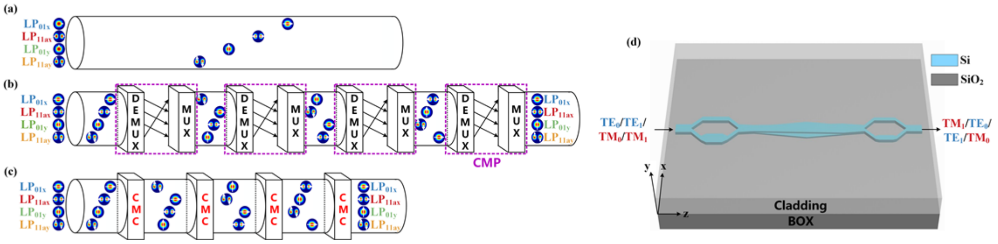

Fig. 1. Schematics of MDM transmission (a) without and with (b) the CMP or (c) the CMC scheme over practical FMF link. (d) 3D schematic of the proposed CMC on an SOI platform.

When a mode is entered into CMC, it will be transmitted through the three converters mentioned above. Whenever the mode passes through one of them, it will be converted to another mode, or keep the original mode unchanged. Figure 2 presents the working principle of the proposed CMC. Based on this conversion process, the $TE_0/TE_1/TM_0/TM_1$ modes input to CMC can eventually be converted into the corresponding four modes, as shown in Fig. 2(a). The working principle of the TE mode-order converter shown in Fig. 2(b) is similar to that of the Mach–Zehnder interferometer (MZI)-based mode converters [20,23], which is called the beam shaping method. Taking the TE_0-to-TE_1 mode conversion as an example, two antiphase TE_0-like modes can combine and produce a TE_1 mode due to their similar mode profiles [26]. We demonstrate the working principle and propose the optimized size in detail in Fig. 2(b). The input TE_0 mode is split into two beams with equal powers and the same phase, and a phase shifter (PS) induces a phase difference of $(2n+1)\pi$ between the two beams during the propagation. In the end, the two antiphase TE_0 modes recombine and generate a TE_1 mode. Similarly, the input TE_1 mode is split into two antiphase beams with equal powers. After passing through the PS, the two TE_0-like modes with the same phase are recombined into a TE_0 mode. Nevertheless, when it comes to TM modes, things are different. In the case that TM_0 or TM_1 mode is input, the PS induces a phase difference of $2n\pi$ between the two beams, so the output mode after recombination will not change. Therefore, our TE mode-order converter can only convert the input TE modes of each order, and will not introduce unexpected conversion to TM modes.

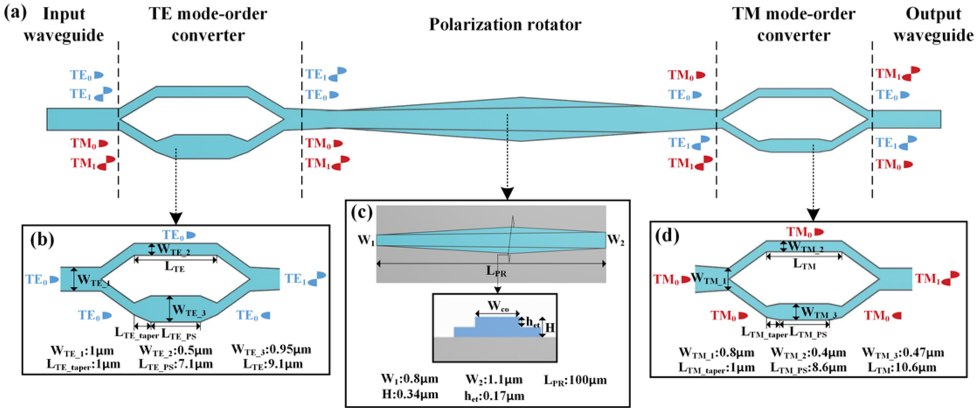

Fig. 2. The working principle of the proposed CMC. (a) The cyclic mode-conversion process in the proposed device. (b) Schematic and working principle of the proposed TE mode-order converter. Take the case of inputting TE_0 mode as an example. (c) Schematic and working principle of the proposed TE_1-TM_0 PR. (d) Schematic and working principle of the proposed TM mode-order converter. Take the case of inputting TM_0 mode as an example.

In this case, two waveguides of the same length are used to establish a differential phase shift using geometric differences in the PS section. The PS consists of adiabatic tapers connected to the input and output waveguides and a wide waveguide in the middle. The function of the adiabatic tapers is to reduce back reflections and maintain the power in the desired mode. The mode effective index changes with the width of the waveguide. Therefore, if the waveguide widths of the upper and lower arm are different, the propagation constants and phase velocities will also be different, which can generate a phase difference. By engineering the power splitting ratio and the structure of PS, the two beams can have equal powers and a specific phase difference. Then the two beams recombine to produce the new mode that we need.

We first study two parallel Si wire waveguides with different widths, as shown in Fig. 3(a). The accumulated phase difference between two waveguides along the section of length L_W is given by

$$\Delta\varphi_1(\lambda) = \frac{2\pi}{\lambda}\left[n_{\mathrm{eff}}(w_1,\lambda) - n_{\mathrm{eff}}(w_0,\lambda)\right] L_W, \tag{1}$$

where w_1 and w_0 are the width of the wide and narrow waveguides, respectively. $n_{\mathrm{eff}}(w_1,\lambda)$ and $n_{\mathrm{eff}}(w_0,\lambda)$ are the effective indexes of the fundamental modes supported by the wide and narrow waveguides, respectively. The free-space wavelength is denoted as λ. Equation (1) shows that the phase shift is mainly controlled by the wavelength, waveguide width, and length of the PS. We need to choose the appropriate w_0, w_1, and L_W to generate a specific phase shift at the design wavelength λ_0. To reduce the loss caused by the mutation of waveguide width, Fig. 3(b) shows the case of introducing a tapered waveguide in the input and output ports. The phase shift generated in the tapered waveguide section can be expressed as

$$\Delta\varphi_2(\lambda) = \frac{2\pi}{\lambda}\int_0^l \{n_{\mathrm{eff}}[w(x),\lambda] - n_{\mathrm{eff}}(w_0,\lambda)\}\,\mathrm{d}x, \tag{2}$$

where x is the length variable of the tapered waveguide. l is the length of the tapered waveguide. w(x) is the waveguide width at x, and the effective index $n_{\mathrm{eff}}[w(x)\cdot\lambda]$ is a compound function of

x. To sum up, the total phase shift value of the designed PS is $\Delta\varphi_1 + 2\Delta\varphi_2$. The phase shifts provided by the PS for TE mode and TM mode are diverse due to the different effective indexes of the two modes [27]. Figure 3(c) shows the relationship between the effective indexes of TE_0 or TM_0 mode and waveguide widths, respectively. Δn_1 or Δn_2 represents the difference of TE_0-like mode or TM_0-like mode effective index between wide and narrow waveguides, respectively. It is worth mentioning that the input and output tapers have little effect in this instance due to their comparatively short lengths, so we first calculate the phase shift introduced by the wide waveguide to TE_0-like mode and TM_0-like mode. Noted that L_{TE} should be as small as possible, we determine the widths of the wide and narrow waveguide to guarantee Δn_1:Δn_2 is 3:2. Substituting into Fig. 3(c), we find that the narrow waveguide width of 0.5 µm and the wide waveguide width of 0.95 µm are proper. The L_{TE} is calculated to be 8.7 µm. Then we transform the input and output part of the wide waveguide into a tapered waveguide and slightly lengthen the length of the tapered part to compensate for the phase shift lost due to the transformation. The optimized size is shown in Fig. 2(b). Compared with the narrow waveguide, the whole TE-PS adds an additional phase shift of 3π to the light wave of TE_0-like mode and an additional phase shift of 2π to the light wave of TM_0-like mode.

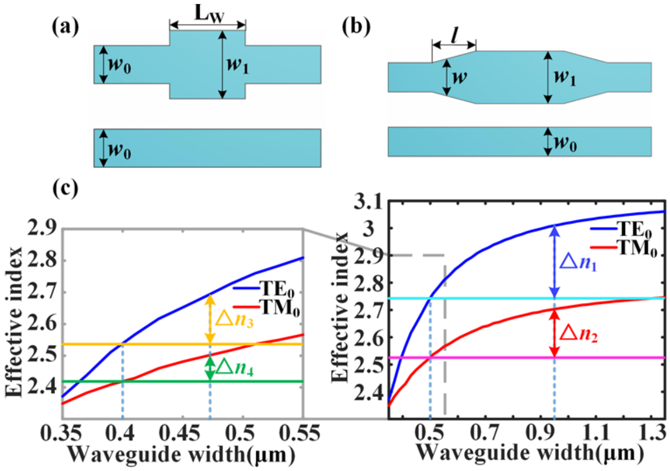

Fig. 3. The cumulative phase difference between two waveguides of different widths without (a) and with (b) tapered waveguides. (c) Relationship between the effective indexes of TE_0 or TM_0 mode and waveguide widths.

The design principle of TE_1-TM_0 PR in the middle part can be referred to [28], which is designed as a bi-level adiabatic tapered waveguide structure, as shown in Fig. 2(c). In the first section, the input strip waveguide gradually changes into a ridge waveguide, creating an environment of asymmetric longitudinal distribution of the refractive index. In some special ranges of ridge width, modes with a similar effective index will generate mode hybridization, such as TE_1 mode and TM_0 mode. The second section gradually changes from ridge waveguide to output strip waveguide to complete mode conversion. Figure 4 shows the variation of the mode effective indexes with the core width when the etching depth is half the height of the top silicon layer. Mode hybridization is observed near $W_{co} = 0.9$ µm, as shown in the marked circle in Fig. 4. In other words, mode hybridization can occur only when the end widths of PR meet the condition of $W_1 < W_{co} < W_2$.

The working principle and optimized size of the TM mode-order converter are shown in Fig. 2(d). The design process is similar to the TE mode-order converter, which will not be repeated here. The whole TM-PS adds an additional phase shift of π to the light wave of TM_0-like

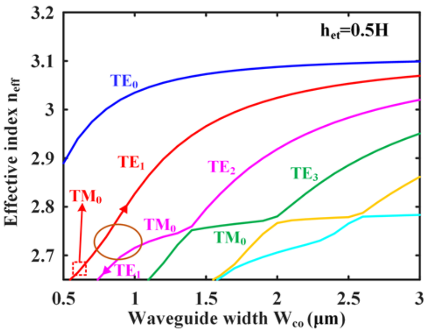

Fig. 4. The calculated effective indexes for the modes of SOI rib waveguide with etching depth het = 0.5H. Here the total height of the Si layer is H = 340 nm.

mode and an additional phase shift of 2π to the light wave of TE_0-like mode compared with the narrow waveguide.

The three-dimensional finite-difference time-domain (3D-FDTD) method is implemented to verify the theoretical results of the device. Figure 5(a) shows the distribution of simulated electric field when four different modes are input to the TE mode-order converter. It can be seen that this device can realize TE_0-TE_1 and TE_1-TE_0 mode conversion simultaneously without affecting each order TM mode. Figure 5(b) shows the distribution of simulated electric field when four different modes are input to PR. This PR can realize the conversion from TE_1 to TM_0 mode (or TM_0 toTE_1 mode) without affecting other input modes. Figure 5(c) shows the main components distribution of the simulated electric field when four different modes are input to the TM mode-order converter. It can be seen that this device we designed can realize TM_0-TM_1 and TM_1-TM_0 mode conversion simultaneously without affecting each order TE mode.

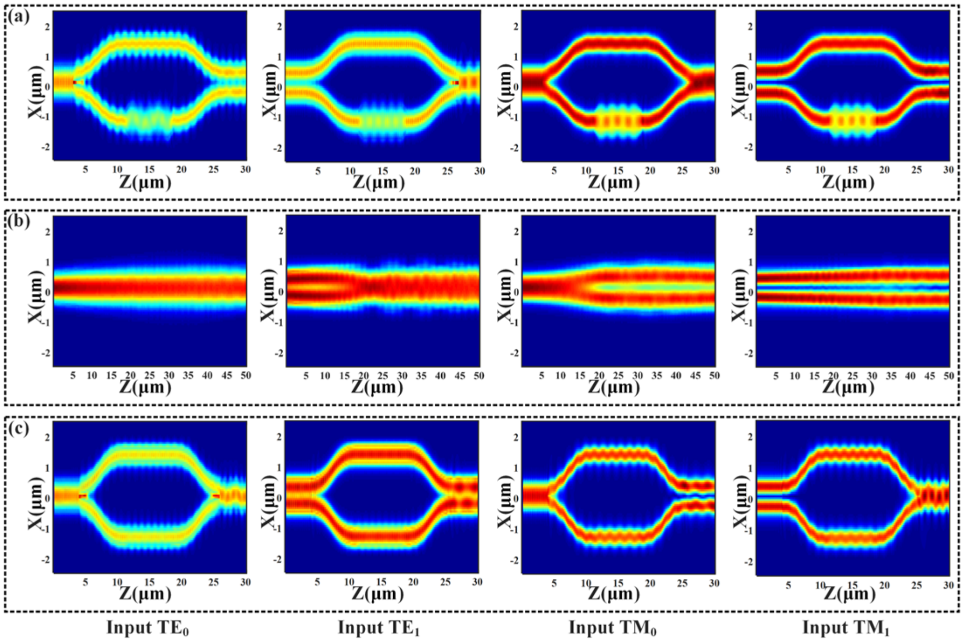

Fig. 5. Distribution of simulated electric field when TE_0/TE_1/TM_0/TM_1 mode is input into (a)TE mode-order converter, (b) TE_1-TM_0 PR, and (c)TM mode-order converter respectively.

By cascading the above three mode converters, a complete cyclic mode conversion process can be realized. Figures 6(a)–6(d) show the simulated electric field distribution. The input $TE_0/TE_1/TM_0/TM_1$ mode can be converted to pure $TM_1/TE_0/TE_1/TM_0$ mode, which agrees well with our previous analysis. Figures 7(a)–7(d) show the simulated transmission spectra under four mode inputs. The insertion loss when each mode input is less than 0.37 dB and the crosstalk is less than −20 dB at the wavelength of 1550 nm. The device has an insertion loss<0.59 dB and the crosstalk less than −15 dB over the whole 100 nm band.

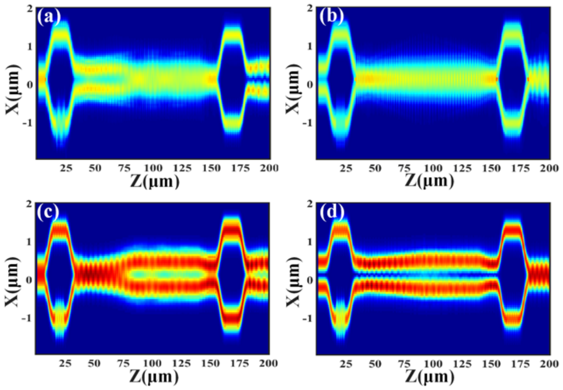

Fig. 6. Distribution of simulated electric field when (a) TE_0 (b) TE_1 (c) TM_0 (d) TM_1 mode is input into the proposed CMC.

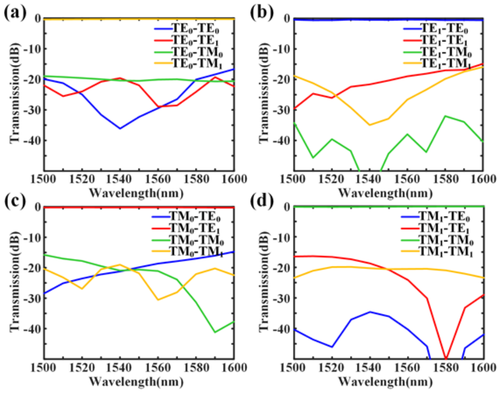

Fig. 7. Simulated transmission spectra when (a) TE_0 (b) TE_1 (c) TM_0 (d) TM_1 mode is input into the proposed CMC.

The tolerance to fabrication errors is also studied using 3D-FDTD simulations. Dimensional errors of $\Delta\delta = \pm 10$ nm are assumed in the width of both phase shifter and narrow waveguides, which is very common in practical fabrication. Figures 8(a)–8(d) show the simulated transmission spectra affected by the fabrication error when each mode input. It is observed that the insertion loss of the device is only degraded to 0.52 dB at the wavelength of 1550 nm, and the operational bandwidth of the device deteriorates slightly. In our device, the simultaneous increase or decrease of the width of the upper and lower arm waveguides will lead to the change of the mode effective indexes in the same direction. Therefore, the phase difference between the two waveguides hardly changes. Moreover, the flat spectral response is achieved even in the presence of dimensional errors as large as ±10 nm, yielding a remarkable tolerance to typical etching errors.

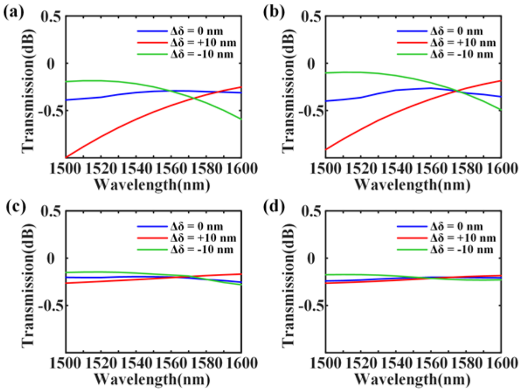

Fig. 8. Simulated insertion loss with dimensional errors of $\Delta\delta = \pm 10\,\text{nm}$ when (a) TE_0 (b) TE_1 (c) TM_0 (d) TM_1 mode is input into the proposed CMC.

3. Fabrication and measurements

The designed CMC has been fabricated on a standard SOI wafer with 340-nm-thick top silicon and 2-μm-thick buried dioxide according to the size of the simulation. First, to form the metal located layer, 1.6-μm-thick PMMA resist was spun on the SOI substrate and the pattern was defined using 100 keV electron beam lithography (EBL, Vistec EBPG5000 + ES). Then, 20 nm Ti (adhesion layer) and 60 nm Au were deposited using thermal evaporation, and a lift-off process was introduced to form the located layer. After that, a 400-nm-thick electron beam resist, AR-P 6200 was used and followed by EBL, and an inductively coupled plasma (ICP, Oxford Plasmalab System 100) etching process was used to transfer the pattern to the silicon layer. The EBL and ICP processes need to be repeated twice due to the need to fabricate the rib waveguides of the polarization rotator. Finally, a 2-μm-thick silica layer had been deposited as the upper cladding using a plasma-enhanced chemical vapor deposition (PECVD, Oxford Plasmalab System 100) process at 300°C. Figure 9(a)–9(d) shows the top-view scanning electron microscope (SEM, GeminiSEM 300) picture of the fabricated CMC, captured before the upper silica cladding was deposited. Figure 9(e) shows the measurement setup used for the characterization of the fabricated CMC. An amplified spontaneous emission (ASE) with a 1.53−1.57 μm wavelength range light source is used in our measurement. The power of the input optical signal is set to 0 dBm. A polarization controller is used to control the polarization state to maximize the coupling efficiency of the grating coupler. We have also fabricated the standardized TE/TM-polarized grating couplers (GC) on the same wafer to couple light between the fibers and the silicon waveguides. The coupling losses are 6.6 and 7.0 dB/port, respectively. The optical signal passing through the polarization controller is coupled with the on-chip GC through the bare fiber fixed on the six-axis displacement platform. The reference mode-(DE)MUX based on asymmetrical directional coupler (ADC) structures are cascaded to conveniently measure the insertion loss and crosstalk of our proposed CMC [29]. The polarization beam splitters (PBS) based on a three-waveguide coupler [30] are used to combine/separate the TE_0 and TM_0 modes while the high-order modes (TE_1, TM_1) are (de)multiplexed by using cascaded ADCs. The on-chip MUX will selectively excite different modes coupled into the CMC, and the on-chip DEMUX is utilized near the receiver side to demultiplex the modes. To compensate for the optical power loss, the received optical signals are amplified by an erbium-doped fiber amplifier (EDFA). A variable optical attenuator (VOA) is used to regulate optical power before detection. An optical spectrum analyzer (OSA, EXFO OSA20) is used to obtain the spectrum of the output optical signal. The fundamental mode of light propagating in fiber is coupled to the input port to generate TE_0 or

TM_0 mode by TE/TM-polarized grating coupler, respectively. The input TE_0 or TM_0 mode will be multiplexed by the MUX into the bus waveguide, which is then converted to the corresponding mode by CMC. Finally, the converted mode will be demultiplexed to the corresponding output port by the DEMUX. Therefore, by measuring the output power spectrum of the mode signal of the corresponding output port and normalizing it according to the reference GCs and the reference mode-(DE)MUX fabricated on the same wafer, the transmission spectrum of CMC can be obtained. Similarly, the unconverted and incorrectly converted modes will be demultiplexed into the other ports as the crosstalk. Table 1 shows the input and output mode signals and their corresponding relationship with ports. Figure 10(a)-(d) depicts the measured transmission spectra of the device at a received optical power of −15 dBm injected with TE_0/TE_1/TM_0/TM_1 modes, respectively, which are normalized according to the reference GCs and the reference mode-(DE)MUX fabricated on the same wafer. Table 2 depicts the measurement performance obtained from the spectrum. It shows that the insertion loss of the CMC for each mode is less than 2.22 dB and the crosstalk is less than −16.2 dB. Limited to the bandwidth range of the on-chip GCs, the coupling loss increases sharply outside the wavelength range of 1540–1560 nm, resulting in the output power being too low to be detected by the OSA. But from the transmission curve trend shown in the experiment, we can definitely predict that the device has a larger bandwidth than 20 nm for each input mode.

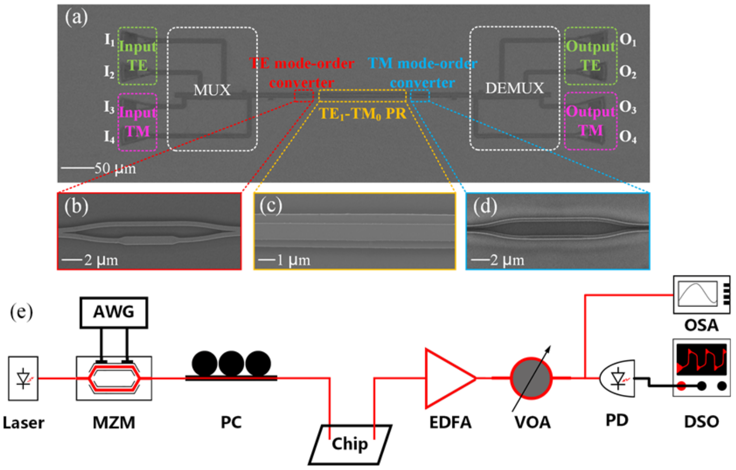

Fig. 9. SEM images of (a) the proposed CMC, (b) the TE mode-order converter, (c) the TE_1-TM_0 PR, and (d) the TM mode-order converter. (e) Experimental setup. AWG, arbitrary waveform generator; MZM, Mach−Zehnder modulator; PC, polarization controller; EDFA, erbium-doped fiber amplifier; VOA, variable optical attenuator; OSA, optical spectrum analyzer; PD, photodiode; DSO, digital storage oscilloscope.

Table 1. Modes signal conversion processes and their correspondence to input and output ports

Input port	Mode excited by multiplexer	Mode converted by CMC	Output port
I_1	TE_1	TE_0	O_2
I_2	TE_0	TM_1	O_4
I_3	TM_0	TE_1	O_1
I_4	TM_1	TM_0	O_3

In order to prove the concept of using the CMC for CMP transmission, we carried out an experimental demonstration of data communications of 80 Gb/s per wavelength using the four

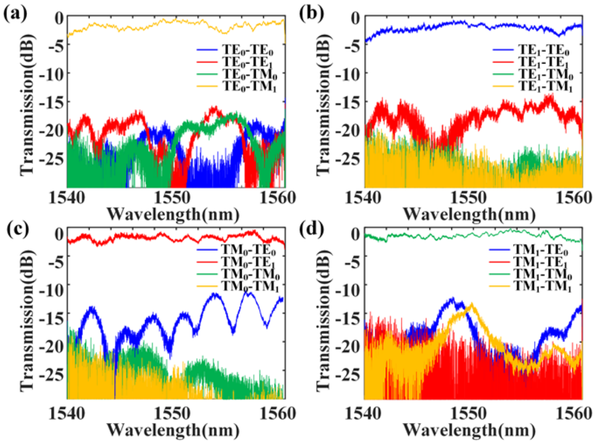

Fig. 10. Measured transmission spectra when (a) TE_0 (b) TE_1 (c) TM_0 (d) TM_1 mode is input into the proposed CMC.

Table 2. Measured performance of the CMC

Mode excited by multiplexer	Insertion Loss @1550 nm (dB)	Crosstalk @1550 nm (dB)	Bandwidth (nm)
TE_0	0.65	−21.3	>20
TE_1	1.92	−16.9	>20
TM_0	2.22	−18.1	>20
TM_1	1.18	−16.2	>20

modes. The 20 Gb/s non-return-to-zero on-off keying (NRZ-OOK) signals are generated by an arbitrary waveform generator (AWG) with a commercial $LiNbO_3$ Mach−Zehnder modulator (MZM). The wavelength of the laser is set at 1550 nm. The received eye diagrams are shown in Fig. 11, indicating that clear and open eye diagrams can be measured at one output port, while the signal from other output ports can be barely detected. These results demonstrate that the CMC can be used for high-speed optical communication applications. Finally, the bit error rate (BER) measurements are performed. The back-to-back case is measured as a reference, and the results are shown in Fig. 12. It can be seen that the measured power penalties are all about 1 dB. It is worth noting that the device can be only measured by one channel at a time due to the limitation of the experimental facility. Fortunately, the fabricated device exhibits very low crosstalk, and the power penalty will not increase markedly if we transmit the signal on all modes at the same time.

Though we cannot measure the geometry directly because of our experimental condition limitation, we can deduce the fabrication error by inspecting the tendency of loss and crosstalk. The insertion loss measured experimentally is normalized according to the reference GCs and the reference mode-(DE)MUX fabricated on the same wafer. In other words, if there are some differences between the performances of the reference (DE)MUX on the same wafer and the (DE)MUX used in our test device, the insertion loss measured in the experiment is not accurate enough, and we think that this is one of the important reasons that the insertion loss in the experiment is higher than that in the simulations. Unfortunately, the ADC-based mode-(DE)MUX is sensitive to fabrication errors, even a deviation of ±10 nm will introduce an additional loss of about 1–2 dB according to our subsequent simulation results. In the fabrication process, such dimensional errors are difficult to avoid, and this may introduce additional loss when calculating insertion loss and crosstalk through the transmission spectrum. Meanwhile, the crosstalk of the device is not as good as the simulation results. Through the simulation of fabrication errors, we

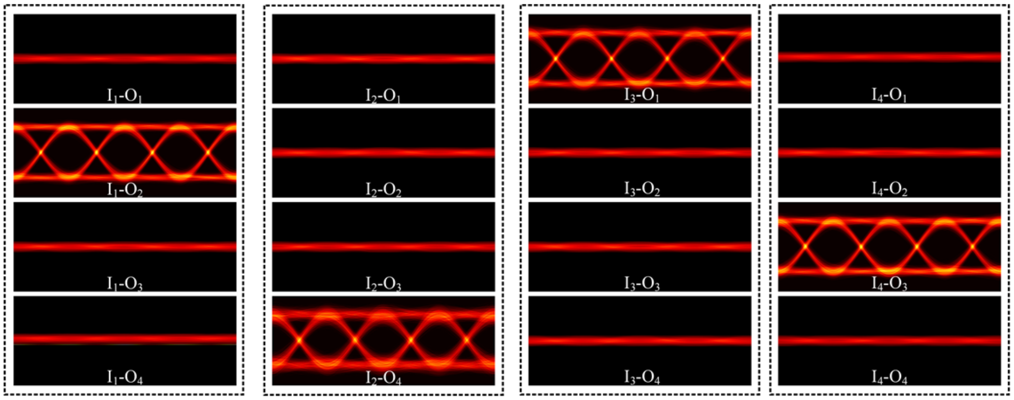

(a) (b) (c) (d)

Fig. 11. (a)-(d) 20 Gb/s eye diagrams at a received optical power of −15 dBm when the signal is input to I_1-I_4 port, respectively.

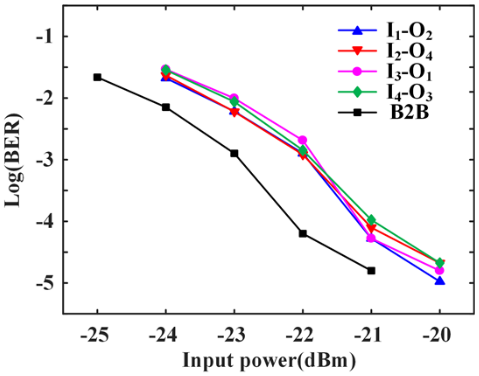

Fig. 12. Measured BER for the back-to-back (B2B) reference case, port I_1 to O_2, port I_2 to O_4, port I_3 to O_1, and port I_4 to O_3 at 1550 nm.

can speculate that the ridge waveguide of PR in the middle of CMC is partially under-etched. The effective indexes of TE and TM modes in ridge waveguide change when choosing different etching depths, and it is obvious that the mode hybridization region shifts correspondingly. One has a smaller W_{co} (where the mode hybridization region locates) when the optical waveguide is under-etched. Particularly, the TM_0 mode becomes leaky when $W_{co}<W_{TE\_1}$ in this case. This results in insufficient mode conversion, which also affects insertion loss and crosstalk performance of our device. The insertion loss and crosstalk can be further reduced by optimizing the fabrication process, such as optimizing the metal marker deposition and lift-off process, using the thermal oxidation method instead of PECVD to form the SiO_2 layer to reduce scattering and reflection, and optimizing the lithography and etching processes for more accurate etching depth and smaller sidewall roughness.

4. Conclusion

In summary, we have proposed and experimentally demonstrated a CMC based on the cascade of mode converters. This device can implement CMP operations on-chip to effectively reduce the impact of DMD and MDL in MDM transmission. We have designed three different mode converters that do not affect the non-target modes. The CMC cascaded by them can convert any of the four input modes. The simulation results show that the insertion loss of each mode of our device is less than 0.59 dB and the crosstalk is lower than −15 dB in the whole C-band. The experimental results confirm that at the central wavelength of 1550 nm, the measured insertion loss is less than 0.65/1.92/2.22/1.18 dB for the converted $TM_1/TE_0/TE_1/TM_0$ modes, respectively. The crosstalk of the CMC for each mode is less than −16.2 dB. The bandwidth range is larger than 20 nm for each input mode. This device is compatible with CMOS fabrication technology and can be easily integrated with other optical components. Furthermore, the tolerance study shows that our device has a large tolerance for fabrication errors. Our device has attractive prospects for deployment to actual MDM links, and we believe that the proposed scheme provides a new solution for long-distance high-capacity MDM transmission.

Funding. National Key Research and Development Program of China (2018YFB1800904); National Natural Science Foundation of China (62171190).

Disclosures. The authors declare no conflicts of interest.

Data availability. Data underlying the results presented in this letter are not publicly available at this time but may be obtained from the authors upon reasonable request.

References

1. T. Morioka, "New generation optical infrastructure technologies: EXAT initiative towards 2020 and beyond," in *2009 14th OptoElectronics and Communications Conference*, pp. 1–2.
2. E. Ip, M.-J. Li, K. Bennett, Y.-K. Huang, A. Tanaka, A. Korolev, K. Koreshkov, W. Wood, E. Mateo, and J. Hu, "146λ× 6× 19-Gbaud wavelength-and mode-division multiplexed transmission over 10× 50-km spans of few-mode fiber with a gain-equalized few-mode EDFA," J. Lightwave Technol. **32**(4), 790–797 (2014).
3. J. V. Weerdenburg, R. Ryf, R. A. Aguirre, N. K. Fontaine, R.-J. Essiambre, H. Chen, J. C. A. Zacarias, R. A. Correa, S. Gross, and N. Riesen, "Mode-multiplexed 16-QAM transmission over 2400-km large-effective-area depressed-cladding 3-mode fiber," in *Optical Fiber Communication Conference* (Optical Society of America, 2018), pp. 1–3.
4. A. Lobato, F. Ferreira, M. Kuschnerov, D. V. D. Borne, S. L. Jansen, A. Napoli, B. Spinnler, and B. Lankl, "Impact of mode coupling on the mode-dependent loss tolerance in few-mode fiber transmission," Opt. Express **20**(28), 29776–29783 (2012).
5. R. Ryf, H. Chen, N. Fontaine, A. V. Benitez, J. A. Lopez, C. Jin, B. Huang, M. B. Astruc, D. Molin, and F. Achten, "10-mode mode-multiplexed transmission over 125-km single-span multimode fiber," in *European Conference on Optical Communication* (Institute of Electrical and Electronics Engineers, 2015), pp. 1–3.
6. N. K. Fontaine, R. Ryf, H. Chen, A. V. Benitez, J. A. Lopez, R. A. Correa, B. Guan, B. Ercan, R. P. Scott, and S. B. Yoo, "30× 30 MIMO transmission over 15 spatial modes," *in Optical Fiber Communication Conference* (Optical Society of America, 2015), p. Th5C. 1.
7. S. Jiang, L. Ma, Z. Zhang, X. Xu, S. Wang, J. Du, C. Yang, W. Tong, and Z. He, "Design and characterization of ring-assisted few-mode fibers for weakly coupled mode-division multiplexing transmission," J. Lightwave Technol. **36**(23), 5547–5555 (2018).
8. Y. Xie, L. Pei, J. Zheng, Q. Zhao, T. Ning, and J. Li, "Design of steering wheel-type ring depressed-core 10-mode fiber with fully improved mode spacing," Opt. Express **29**(10), 15067–15077 (2021).
9. Y. Xie, L. Pei, J. Zheng, T. Ning, J. Li, B. Ai, and R. He, "Design and characterization of nanopore-assisted weakly-coupled few-mode fiber for simpler MIMO space division multiplexing," IEEE Access **8**, 76173–76181 (2020).
10. K. Shibahara, T. Mizuno, H. Kawakami, T. Kobayashi, M. Nakamura, K. Shikama, K. Nakajima, and Y. Miyamoto, "Full C-band 3060-km DMD-unmanaged 3-mode transmission with 40.2-Tb/s capacity using cyclic mode permutation," J. Lightwave Technol. **38**(2), 514–521 (2020).
11. A. E. Willner, H. Huang, Y. Yan, Y. Ren, N. Ahmed, G. Xie, C. Bao, L. Li, Y. Cao, and Z. Zhao, "Optical communications using orbital angular momentum beams," Adv. Opt. Photonics **7**(1), 66–106 (2015).
12. T. A. Birks, I. G. Sánchez, S. Yerolatsitis, S. L. Saval, and R. R. Thomson, "The photonic lantern," Adv. Opt. Photonics **7**(2), 107–167 (2015).
13. N. K. Fontaine, H. Chen, M. Mazur, L. Dallachiesa, K. Kim, R. Ryf, D. Neilson, and J. Carpenter, "Hermite-Gaussian mode multiplexer supporting 1035 modes," in *Optical Fiber Communication Conference* (Optical Society of America, 2021), pp. 1–3.
14. Y. He, Y. Zhang, Q. Zhu, S. An, R. Cao, X. Guo, C. Qiu, and Y. Su, "Silicon high-order mode (de) multiplexer on single polarization," J. Lightwave Technol. **36**(24), 5746–5753 (2018).
15. Y. Liu, Z. Zhong, S. Wang, Y. Liu, Y. Yao, J. Du, Q. Song, and K. Xu, "Four-mode waveguide crossing via digitized meta-structure," in *Optical Fiber Communication Conference* (Optical Society of America, 2021), pp. 1–3.
16. D. Liu, L. Zhang, H. Jiang, and D. Dai, "High-performance silicon quadplexer for passive optical networks," in *Optical Fiber Communication Conference* (Optical Society of America, 2021), pp. 1–3.

17. H. Xu, C. Liu, D. Dai, and Y. Shi, “Direct-access mode-division multiplexing switch for scalable on-chip multi-mode networks,” Nanophotonics **10**(18), 4551–4566 (2021).
18. C. Sun, W. Wu, Y. Yu, X. Zhang, and G. T. Reed, “Integrated tunable mode filter for a mode-division multiplexing system,” Opt. Lett. **43**(15), 3658 (2018).
19. Z. Cheng and H. K. Tsang, “Experimental demonstration of polarization-insensitive air-cladding grating couplers for silicon-on-insulator waveguides,” Opt. Lett. **39**(7), 2206 (2014).
20. C. Sun, Y. Yu, G. Chen, and X. Zhang, “On-chip switch for reconfigurable mode-multiplexing optical network,” Opt. Express **24**(19), 21722–21728 (2016).
21. Y. Ding, J. Xu, F. D. Ros, B. Huang, H. Ou, and C. Peucheret, “On-chip two- few-mode fibers using tapered directional coupler-based mode multiplexer and demultiplexer,” Opt. Express **21**(8), 10376–10382 (2013).
22. Y. Li, C. Li, C. Li, B. Cheng, and C. Xue, “Compact two-mode (de) multiplexer based on symmetric Y-junction and multimode interference waveguides,” Opt. Express **22**(5), 5781–5786 (2014).
23. B.-T. Lee and S.-Y. Shin, “Mode-order converter in a multimode waveguide,” Opt. Lett. **28**(18), 1660–1662 (2003).
24. T. Wang, H. Guo, H. Chen, J. Yang, and H. Jia, “Ultra-compact reflective mode converter based on a silicon subwavelength structure,” Appl. Opt. **59**(9), 2754–2758 (2020).
25. Y. Zhao, X. Guo, Y. Zhang, J. Xiang, K. Wang, H. Wang, and Y. Su, “Ultra-compact silicon mode-order converters based on dielectric slots,” Opt. Lett. **45**(13), 3797–3800 (2020).
26. D. Chen, X. Xiao, L. Wang, Y. Yu, W. Liu, and Q. Yang, “Low-loss and fabrication tolerant silicon mode-order converters based on novel compact tapers,” Opt. Express **23**(9), 11152–11159 (2015).
27. H. Fukuda, K. Yamada, T. Tsuchizawa, T. Watanabe, H. Shinojima, and S.-I. Itabashi, “Silicon photonic circuit with polarization diversity,” Opt. Express **16**(7), 4872–4880 (2008).
28. D. Dai, Y. Tang, and J. E. Bowers, “Mode conversion in tapered submicron silicon ridge optical waveguides,” Opt. Express **20**(12), 13425–13439 (2012).
29. J. Wang, S. He, and D. Dai, “On-chip silicon 8-channel hybrid (de) multiplexer enabling simultaneous mode-and polarization-division-multiplexing,” Laser Photonics Rev. **8**(2), L18–L22 (2014).
30. D. Dai, “Silicon polarization beam splitter based on an asymmetrical evanescent coupling system with three optical waveguides,” J. Lightwave Technol. **30**(20), 3281–3287 (2012).